Progress In Electromagnetics Research, Vol. 166, 167–175, 2019

High-Sensitivity and Temperature-Insensitive Refractometer Based on TNHF Structure for Low-Range Refractive Index Measurement

Fang Wang[1, 3], Kaibo Pang[1], Tao Ma[1, 3], Xu Wang[1, 3], and Yufang Liu[2, 3, *]

Abstract—Refractive index (RI) measurements find extensive use in biochemical sensing field. However, currently available RI sensors exhibit excessive temperature crosstalk and have low sensitivity in the low RI range. To solve this, a high-sensitivity and temperature-insensitive refractometer based on a tapered no-core-hollow-core fiber (TNHF) structure is proposed for low-range RI measurement. The TNHF comprises two Mach-Zehnder interferometers that are introduced within the tapered no-core fiber and hollow-core fiber, thereby establishing a composite interference. The results of an experimental evaluation demonstrate that maximum sensitivities of 482.74 nm/RIU within an RI range of $1.335 \sim 1.3462$ can be achieved, which is greater than that achieved using a traditional modal interferometer structure. Significantly, the refractometer exhibits ultra-low temperature sensitivities of 0.062 dB/°C and 6.5 pm/°C, which can alleviate the temperature crosstalk. The refractometer can be realistically applied in many fields requiring high precision RI measurement due to its advantages of low cost, ease of manufacture, high sensitivity, and temperature insensitivity.

1. INTRODUCTION

Refractive index (RI) measurements are widely used in biological reactions, chemical experiments, and environmental monitoring [1–3]. Fiber optic RI sensors are widely used for their unique advantages such as compact structure, high-resolution detection, excellent aging characteristics, ability to work in chemically hazardous environments, and inherent resistance to external electromagnetic interference [4, 5]. At present, a variety of fiber optic sensors, such as Mach-Zehnder interferometer (MZI) [6–17], Fabry-Perot interferometer [18, 19], optical fiber grating sensors [20, 21], and surface plasmon resonance [22, 23] are used. Among them, MZI-based sensors have been widely studied due to their low manufacturing cost and simple structure. The structure for MZI sensors can be achieved by utilizing various fiber types, such as microfiber [8], multimode [9, 10], photonic crystal fiber (PCF) [11, 12], or fabrication techniques, such as core mismatch [13, 14], tapering [15, 16], and different type fiber splicing [17]. The higher order modes in the cladding are excited by the mismatch of the mode fields. This unique coupling has the advantages of high sensitivity and fast response to changes in RI and solution concentration. Therefore, RI detection can be achieved by monitoring the interference spectrum.

RI sensors based on different MZI structures have been proposed. Wang et al. fabricated a sensor based on a tapered multimode fiber structure [6], and Chen et al. employed an S-tapered fiber probe to measure the RI [16]. The sensitivities of these optic fiber MZI structures can reach hundreds or even thousands of nm/RIU, but the minimum RI-value limit is above 1.40, which is close to the RI of optical fibers. Further, the high temperature cross-sensitivity (more than 10 pm/°C) of these devices

Received 23 October 2019, Accepted 6 January 2020, Scheduled 16 January 2020

* Corresponding author: Yufang Liu (liuyufang2005@126.com).

[1] College of Electronic and Electrical Engineering, Henan Normal University, 46 Construction East Road, Xinxiang 453007, China. [2] College of Physics and Material Science, Henan Normal University, 46 Construction East Road, Xinxiang 453007, China. [3] Key Laboratory Optoelectronic Sensing Integrated Application of Henan Province, Xinxiang 453007, China.

results in considerable crosstalk in the measurement of RI. Temperature cross-sensitivity is a significant factor in RI measurement, and high temperature cross-sensitivity reduces the sensor detection limit [24]. Therefore, the cross-sensitivity should be minimized while increasing the sensitivity of the sensor.

This paper proposes a high-sensitivity and temperature-insensitive RI sensor for low RI ranges, based on tapered no-core-hollow-core fiber (TNHF) sandwiched between two single-mode fibers (SMFs), and constituting two cascaded MZIs. The tapered no-core fiber (NCF) makes it easy to leak light into the surrounding environment. Hence, this resultant composite interference is easily affected by the surrounding RI (SRI), which ultimately leads to a change with the interference dip in the transmission spectrum. The proposed structure has a simple structure and good repeatability for fabrication, and demonstrates a competitive RI sensitivity of 482.74 nm/RIU within a low RI range from 1.335 to 1.3462. Meanwhile, the temperature-induced cross sensitivity in actual RI measurements can be alleviated owing to the ultra-low temperature sensitivities of 6.5 pm/°C.

2. FABRICATION AND PRINCIPLE

A schematic diagram of the proposed TNHF refractometer is displayed in Fig. 1. The structure includes a section of tapered NCF concatenated to a hollow-core fiber (HCF). The NCF is machined, and the diameter is reduced from 125 µm to 37 µm. The inset of Fig. 1 shows an image of the splicing point of the NCF and HCF under an optical microscope. A short, collapsed region can be clearly seen in this inset. The HCF has an air channel and a silica cladding with diameters of approximately 45 µm and 125 µm, respectively.

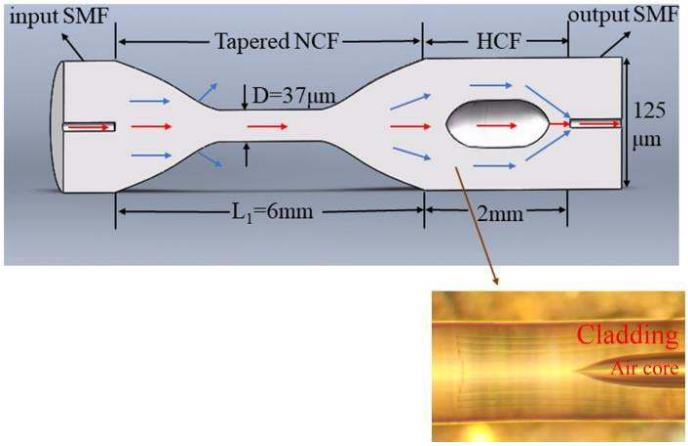

Figure 1. Schematic diagram of the TNHF structure. Inset is a microscopic image of the splicing point of the NCF and HCF.

For the fabrication, first, a segment of SMF and a segment of NCF with a length of 2 mm were coaxially spliced together using a commercial fusion splicer (KL-280G, JiLong) equipped with a built-in SMF splicing program. Then, the HCF with an identical length was coaxially spliced with NCF and another segment of SMF. The coating layer of the NCF was removed using acetone before the splicing process. After splicing, the input SMF and output SMF were connected to a semiconductor optical amplifier (SOA) and an optical spectrum analyzer (OSA), respectively. Fig. 2 displays the flame-based tapering machine image (OC-2020, JiLong) used for the sensor fabrication. The fiber was clamped on two linear motorized stages, and the NCF was expected to be placed directly below the flame nozzle. Hydrogen-oxygen mixed gas was fed into the nozzles. Then, the travel distance, speed of each stage, and preheat time were independently set via the tapering control software. The transmission spectrum of the TNHF can be observed online in the process of tapering.

Figure 3 demonstrates the transmission spectra of four different optical fiber structures, which were monitored during the fabrication process. Clearly, there is no interference pattern of the SMF-no-core-SMF (SNS) structure, and the resultant effect is relatively weak in the SMF-hollow-core-SMF (SHS)

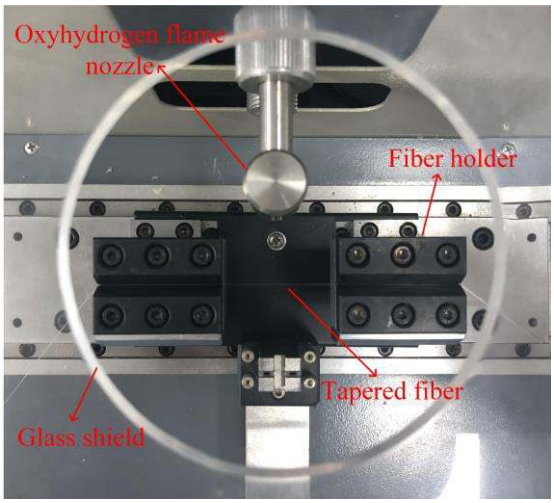

Figure 2. The flame-based tapering machine.

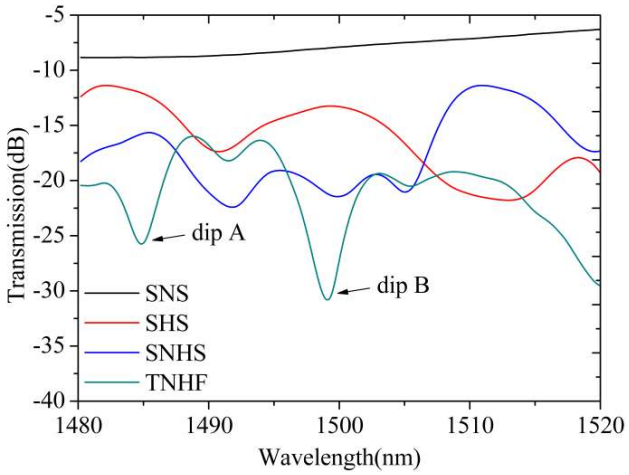

Figure 3. Transmission spectra of the four different optical fiber structures.

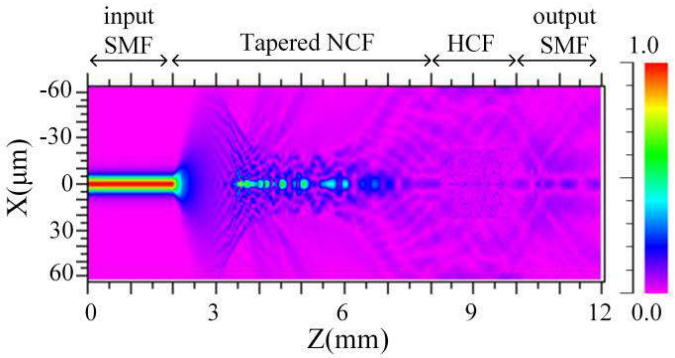

Figure 4. Simulated optical field intensity distribution within the TNHF ($L_1 = 6\,\text{mm}$, $D = 37\,\mu\text{m}$).

structure. By splicing the NCF and HCF together, there are several interference dips, but with an ultra-low extinction ratio (ER). Finally, two interference dips with a relatively high ER (more than 10 dB) were clearly observed in the transmission spectra of the TNHF, which was fabricated by tapering the diameter of the NCF to 37 μm in the SNHS structure. In this paper, considering the effect of ER and mechanical stability in actual measurements, the appropriate diameter to form an effective composite interference should be in the region of 37 μm based on the results of aforementioned experiments. The transmission spectrum of the TNHF shows two distinct interference dips, which is an ideal choice for an MZI structure sensor, and the wavelength shift of two interference dips with higher ER can be observed more obviously in the process of parameter measurement.

A numerical simulation using the beam propagation method (BPM) was used to describe the optical field distribution within the TNHF structure ($L_1 = 6\,\text{mm}$, $D = 37\,\mu\text{m}$), as implemented in the Rsoft software. The simulation parameters are given as follows: the taper waist diameter and RI of NCF were chosen as 37 μm and 1.444; the diameters of air channel and cladding of HCF were 45 μm and 125 μm; the RI of HCF and air were respectively set as 1.444 and 1.0; and the length of taper area was 6 mm. When the input light wavelength was set to 1550 nm, the field intensity distribution along the TNHF in the air was as shown in Fig. 4. When the light propagates through the tapered area, most of it passes through the NCF while a small portion of it leaks out from the fiber. The fundamental mode of the NCF was partly coupled to the high-order mode to ensure that the powers of the modes participating in the interference would be matched better and that the mode interference would be enhanced [6].

Interestingly, when the interference light propagated to the splicing point of NCF and HCF, the light was mainly transmitted to the silica region of the HCF and was guided along this region instead of being confined to the central air channel, which results from the collapsed region between the NCF and HCF; at the second collapsed region, the split modes are recombined into the output SMF. The two collapsed regions around the splicing interfaces play the roles of splitting and combining couplers, as illustrated in Fig. 1. Finally, a portion of light from the HCF is transmitted into the core of the output SMF, which can be detected by an OSA.

As analyzed previously, the TNHF is composed of two cascaded MZIs, and the entire process of light interference can be divided into two steps. The light from the source initially propagates along the core of the input SMF in the fundamental mode. When the light enters the NCF section, a series of high-order modes are effectively excited due to the mode field mismatch between the SMF and NCF. The input light field can be expressed as [25]:

$$E(r,0) = \sum_{m=1}^{M} \eta_m \psi_m(r) \tag{1}$$

where ψ_m is the field profile of high-order mode excited within the NCF, which is determined by the RI and diameter of the fiber core and cladding. The excitation coefficient for each mode (η_m) can be expressed as:

$$\eta_m = \frac{\int_0^\infty E(r,0)\psi_m(r) r dr}{\int_0^\infty \psi_m(r)^2 r dr} \tag{2}$$

Therefore, the distribution of the light field in the direction of light propagation, z, can be expressed as:

$$E(r,z) = \sum_{m=1}^{M} \eta_m \psi_m(r) \exp(j\beta_m z) \tag{3}$$

where β_m is the propagation constant of the excited mth order mode.

Then, when the light passes through the tapered NCF, due to the differences in effective RIs between fundamental mode and high-order modes and the optical path difference of the light signals in transmission, interference between the high-order modes and the fundamental mode occurs, and thus an MZI is formed. The transmission intensity can be analyzed by using the two-wave interference model for simplification [17, 26]:

$$I_1 = I_f + I_m + 2\sqrt{I_f I_m}\cos\varphi_m \tag{4}$$

where I_f and I_m are the intensities of the fundamental mode and mth high-order mode, respectively. The phase difference φ_m between the fundamental mode and the mth high-order mode can be expressed as:

$$\varphi_m = \frac{2\pi \Delta n_{eff}^m L_1}{\lambda} \tag{5}$$

where the effective interference length of the 1st tapered area is L_1; λ is the wavelength of input light; and Δn_{eff}^m represents the effective RI difference between the modes. The mth order interference dip wavelength of the spectrum can be described as:

$$\lambda_m = \frac{2\Delta n_{eff}^m L_1}{2m+1} \tag{6}$$

When the interference light reaches the splicing point of NCF and HCF, a part of the beam passes through the air core, and another part travels along the silica cladding. After propagating through the HCF, the two separated beams are coupled in the output SMF. Due to the differences in effective RIs between the air and the silica cladding and the optical path difference between the light signals in transmission, an interference exists between the propagating fundamental and high-order mode, and thus, an MZI is formed. The intensity of output light from the HCF section also uses a two-wave interference model:

$$I_2 = I_{\text{output}} = I_1 + I_n + 2\sqrt{I_1 I_n}\cos\varphi_n \tag{7}$$

where I_n is the intensities of the fundamental mode and nth high-order mode, and φ_n is the phase difference between the interference modes. The nth order interference dip wavelength of the spectrum can be expressed as:

$$\lambda_n = \frac{2\Delta n_{eff}^n L_2}{2n+1} \tag{8}$$

where L_2 is the length of the effective interference region of the HCF section, and Δn_{eff}^n is the effective refractive index difference between interference modes in the HCF.

Therefore, the light transmitted from the output SMF is the composite interference based on the two cascaded MZIs. Δn_{eff}^n would be altered as the SRI changes on account of different modes have different responses to the SRI variation. Based on Eq. (8), the SRI change of the TNHF can be measured by monitoring the wavelength of the transmission spectrum.

3. EXPERIMENTS AND DISCUSSION

3.1. Refractive Index Experiment

Figure 5 shows the experimental setup for RI measurement. To prevent the fiber from bending, the fabricated TNHF is stably and horizontally fastened on a glass slide by using UV glue. Broadband light from an SOA (KG-SOA-C-10-D-FA, Conquer) (wavelength range of 1200–1700 nm) was coupled to the input SMF of the TNHF structure, and the output optical spectral signal was interrogated using a high-resolution (0.02 nm) OSA (MS9740A, Anritsu, Japan). The SRI response of the TNHF structure was investigated by immersing the sensor in different aqueous NaCl solutions with RIs ranging from 1.335 to 1.3462, while the temperature was maintained at 20°C. After recording transmission spectrum,

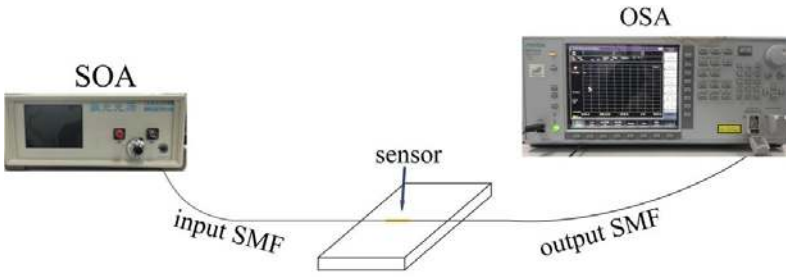

Figure 5. Schematic diagram of the experimental setup for RI measurement.

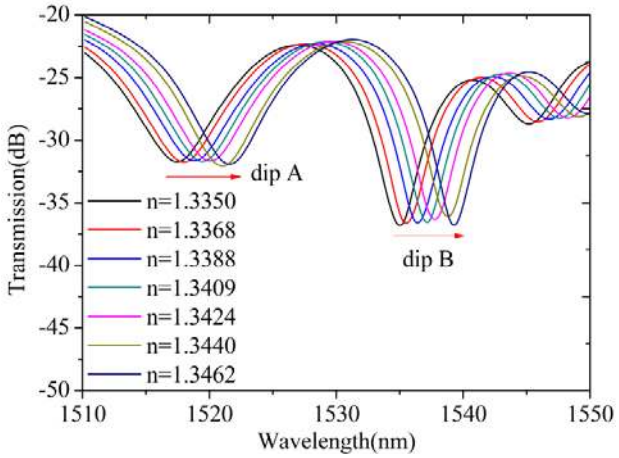

Figure 6. Transmission spectrum evolution when SRI is changed.

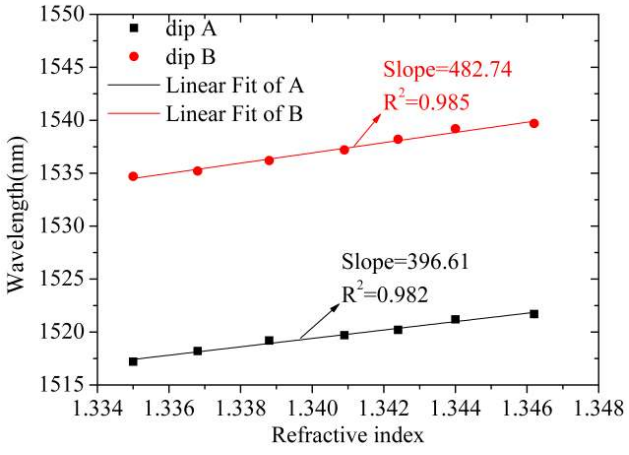

Figure 7. Wavelength shift of dips A and B with the variation of the SRI.

deionized water was used to clean TNHF, recovering the original spectrum in air. Subsequently, the TNHF was immersed in a solution with a different RI to record a new transmission spectrum. To ensure spectral stability, each new spectrum is immersed for 3 minutes before being recorded.

Figure 6 exhibits the measured output spectral evolution of the proposed sensor in the range of $1.335 \sim 1.3462$. To depict and analyze the spectra change, we trace the interference of dips A and B. As can be seen, with increasing SRI, both interference dips A and B exhibit a resonant red shift of wavelength, which is due to the increase of effective RI difference between the interference modes.

The relationships between the SRI increment and wavelength responses of dips A and B are shown in Fig. 7. For dip A, the RI sensitivity during the increasing processes was determined to be 396.61 nm/RIU, with R^2 being 0.982. For dip B, the corresponding RI sensitivity was determined to be 482.74 nm/RIU, with R^2 being 0.985. Both the fitting curves exhibit excellent linearity with high linear regression coefficient values (R^2). According to the experimental results, the TNHF is sufficiently sensitive to the SRI in the low RI range.

3.2. Temperature Experiment

The temperature response characteristics of the proposed sensor were analyzed by fixing the fabricated sensor unit (TNHF interferometer) to a temperature control box and varying the temperature from 25°C to 50°C in steps of 5°C. Fig. 8 displays the transmission spectra of the TNHF at different temperatures. As the external temperature increases, the interference wavelengths of dips A and B barely shift, even though their respective intensities increase by -0.302 dB and 1.512 dB.

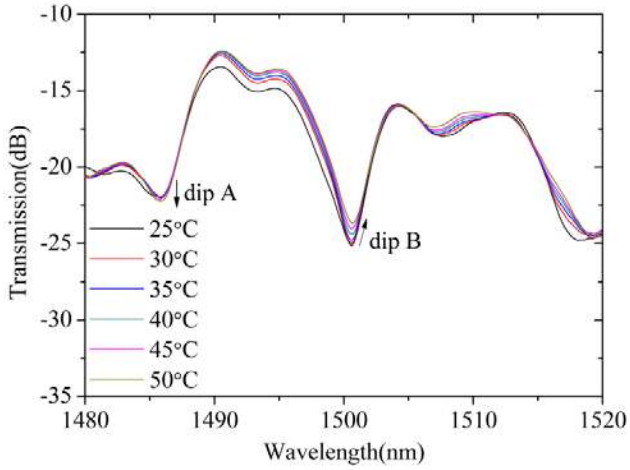

Figure 8. Transmission spectra of the TNHF at different temperatures.

The intensity variations and wavelength shift of the interference dips are shown in Figs. 9(a) and 9(b), respectively. It can be seen that the respective temperature sensitivities of -0.012 dB/°C and 0.062 dB/°C of dips A and B (R^2 approaching 0.997 and 0.983) are obtained in the range of $25 \sim 50$°C, from Fig. 9(a). Meanwhile, the center wavelength shifts of dips A and B are less than 0.02 nm and 0.16 nm, respectively, in the long-wave direction, as shown in Fig. 9(b). For dip B, the temperature sensitivity is 6.5 pm/°C, with R^2 being 0.971. This may be the result of a combination of temperature induced effective RI change and thermal expansion induced axial strain variation in the TNHF. The former drives the spectrum to move toward longer wavelengths, while the latter pulls it back, causing the two effects to cancel each other out. Compared with the transmission spectrum change induced by the SRI, the ultra-weak temperature response of the TNHF can be neglected, thus sufficiently resolving the temperature crosstalk problem. Therefore, the proposed sensor of TNHF structure is extremely suitable for accurately measuring minute SRI changes over a wide temperature range.

Table 1 shows a comparison between the proposed sensor and previously developed MZI-based RI fiber-optic sensors. Compared with other examples, the TNHF is easier and has lower cost to

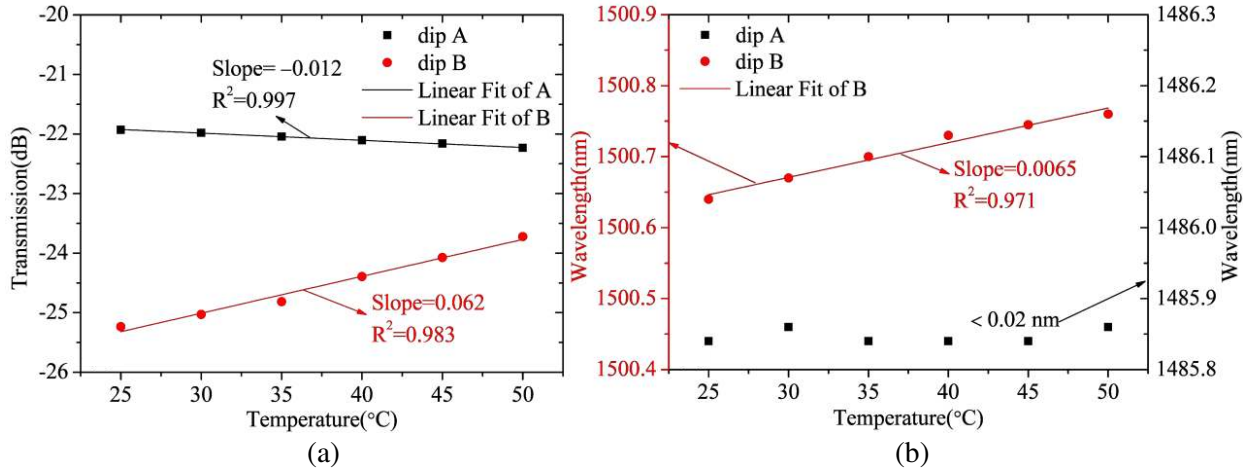

Figure 9. (a) Intensities of dips A and B change with temperature; (b) Wavelength shift of dips A and B with the variation of the temperature.

Table 1. Comparison of the proposed TNHF with other RI sensors.

Sensor structure	RI/temperature sensitivity	RI range	Reference
SMF-NCF-SMF	259 nm/RIU	1.333 ∼ 1.381	[27]
S-tapered fiber probe	1882.4 nm/RIU	1.4216 ∼ 1.4284	[16]
Tapered multimode fiber	∼ 1900 (maximum) (at a RI of 1.44)	1.33 ∼ 1.44	[6]
S-tapered PCF	125 nm/RIU and 4.2 pm/°C	1.38 ∼ 1.44	[12]
SMF-MMF-SMF	188 nm/RIU	1.342 ∼ 1.352	[28]
Down-taper-TCF	−79.335 nm/RIU and 65 pm/°C	1.336 ∼ 1.351	[7]
Sb_2Te_3 topological insulator: surface plasmon resonance	88.5°/RIU and 15.8/RIU (Normalized reflection)	1.331 ∼ 1.350	[22]
The proposed TNHF	482.74/RIU and 6.5 pm/°C	1.3386 ∼ 1.3479	Our work

manufacture than the RI sensing system based on SPR in [22]. Our work is based on wavelength demodulation with a high linear regression coefficient values in the low RI range of 1.335 ∼ 1.3462, avoiding the error caused by the unstable power of the light source with demodulation based on intensity in actual measurements. Furthermore, our work also avoids the dangerous chemical corrosion of [28]. The TNHF sensor provides superior RI sensitivity in lower RI ranges and exhibits an ultra-low temperature crosstalk. The high sensitivity in the low RI range can potentially enable the development of miniaturized and high-sensitivity sensors suitable for chemical and biological applications.

4. CONCLUSION

In conclusion, this study proposes and experimentally evaluates a novel RI sensor having high RI sensitivity and ultra-low temperature crosstalk. Based on a TNHF structure, the sensor consists of a tapered NCF cascaded with an HCF. The TNHF structure provides two cascaded MZIs, which are introduced within the tapered NCF and HCF, and based on which, composite interference is established. The experimental results show that the sensor can achieve maximum sensitivities of 482.74 nm/RIU in the low RI range of 1.335 ∼ 1.3462. In addition, it exhibits an ultra-low sensitivity to temperature variation (6.5 pm/°C and 0.062 dB/°C). Compared with the transmission spectrum change induced by the SRI, the ultra-weak temperature response of the TNHF can be neglected, thus sufficiently resolving the temperature crosstalk problem. The proposed sensor of TNHF structure is a suitable candidate in the biochemical and physical sensing fields.

ACKNOWLEDGMENT

This work was supported by the National Natural Science Foundation of China (Grant No. 61627818), the Scientific and Technological Project of Henan Province (Grant No. 182102210367), the Key Project of Henan Education Department (Grant No. 19A510002), and the Cultivation Foundation of Henan Normal University National Project (Grant Nos. 2017PL04 and 5101239170010).

REFERENCES

1. Caucheteur, C., T. Guo, and J. Albert, "Review of plasmonic fiber optic biochemical sensors: Improving the limit of detection," *Anal. Bioanal. Chem.*, Vol. 407, No. 14, 3883–3897, 2015.
2. James, S. W., S. Korposh, S. Lee, and R. P. Tatam, "A long period grating-based chemical sensor insensitive to the influence of interfering parameters," *Opt. Express*, Vol. 22, No. 7, 8012–8023, 2014.
3. Tian, Z., S. S. H. Yam, J. Barnes, W. Bock, P. Greig, J. M. Fraser, H. P. Loock, and R. D. Oleschuk, "Refractive index sensing with Mach-Zehnder interferometer based on concatenating two single-mode fiber tapers," *IEEE Photonics Technol. Lett.*, Vol. 20, No. 8, 626–628, 2008.
4. Wang, J., Y. Jin, Y. Zhao, and X. Dong, "Refractive index sensor based on all-fiber multimode interference," *Optik*, Vol. 124, No. 14, 1845–1848, 2013.
5. Wang, Q., B. T. Wang, L. X. Kong, and Y. Zhao, "Comparative analyses of bi-tapered fiber Mach-Zehnder interferometer for refractive index sensing," *IEEE Trans. Instrum. Meas.*, Vol. 66, No. 9, 2483–2489, 2017.
6. Wang, P., G. Brambilla, M. Ding, Y. Semenova, Q. Wu, and G. Farrell, "High-sensitivity, evanescent field refractometric sensor based on a tapered, multimode fiber interference," *Opt. Lett.*, Vol. 36, No. 12, 2233–2235, 2011.
7. Sun, L., J. Qin, Z. Tong, W. Zhang, and M. Gong, "Simultaneous measurement of refractive index and temperature based on down-taper and thin-core fiber," *Opt. Commun.*, Vol. 426, 506–510, 2018.
8. Wo, J., G. Wang, Y. Cui, Q. Sun, R. Liang, P. Shum, and D. Liu, "Refractive index sensor using microfiber-based Mach-Zehnder interferometer," *Opt. Lett.*, Vol. 37, No. 1, 67–69, 2012.
9. Wang, H., H. Meng, R. Xiong, Q. Wang, B. Huang, X. Zhang, W. Yu, C. Tan, and X. Huang, "Simultaneous measurement of refractive index and temperature based on asymmetric structures modal interference," *Opt. Commun.*, Vol. 364, 191–194, 2016.
10. Lee, B., Y. Kim, K. Park, J. Eom, M. Kim, B. Rho, and H. Choi, "Interferometric fiber optic sensors," *Sensors*, Vol. 12, No. 3, 2467–2486, 2012.
11. Ahmed, F., V. Ahsani, L. Melo, P. Wild, and M. B. G. Jun, "Miniaturized tapered photonic crystal fiber Mach-Zehnder interferometer for enhanced refractive index sensing," *IEEE Sens. J.*, Vol. 16, 8761–8766, 2016.
12. Shi, F., J. Wang, Y. Zhang, Y. Xia, and L. Zhao, "Refractive index sensor based on S-tapered photonic crystal fiber," *IEEE Photonics Technol. Lett.*, Vol. 25, No. 4, 344–347, 2013.
13. Lu, H., X. Wang, S. Zhang, F. Wang, and Y. Liu, "A fiber-optic sensor based on no-core fiber and Faraday rotator mirror structure," *Opt. Laser Technol.*, Vol. 101, 507–514, 2018.
14. Cao, Y., H. Liu, Z. Tong, S. Yuan, and J. Su, "Simultaneous measurement of temperature and refractive index based on a Mach-Zehnder interferometer cascaded with a fiber Bragg grating," *Opt. Commun.*, Vol. 342, 180–183, 2015.
15. Yang, R., Y. S. Yu, Y. Xue, C. Chen, Q. D. Chen, and H. B. Sun, "Single S-tapered fiber Mach-Zehnder interferometers," *Opt. Lett.*, Vol. 36, No. 23, 4482–4484, 2011.
16. Chen, C., R. Yang, X. Y. Zhang, W. H. Wei, Q. Guo, X. Zhang, L. Qin, Y. Q. Ning, and Y. S. Yu, "Compact refractive index sensor based on an S-tapered fiber probe," *Opt. Mater. Express*, Vol. 8, No. 4, 919–925, 2018.

17. Lu, C., J. Su, X. Dong, T. Sun, and K. T. V. Grattan, "Simultaneous measurement of strain and temperature with a few-mode fiber-based sensor," *J. Lightwave Technol.*, Vol. 36, No. 13, 2796–2802, 2018.
18. Tian, J., Z. Lu, M. Quan, Y. Jiao, and Y. Yao, "Fast response Fabry-Perot interferometer microfluidic refractive index fiber sensor based on concave-core photonic crystal fiber," *Opt. Express*, Vol. 24, No. 18, 20132–20142, 2016.
19. Gao, S., W. Zhang, Z.-Y. Bai, H. Zhang, W. Lin, L. Wang, and J. Li, "Microfiber-enabled in-line Fabry-Pérot interferometer for high-sensitive force and refractive index sensing," *J. Lightwave Technol.*, Vol. 32, No. 9, 1682–1688, 2014.
20. Coelho, L., D. Viegas, J. L. Santos, and J. M. M. M. Almeida, "Characterization of zinc oxide coated optical fiber long period gratings with improved refractive index sensing properties," *Sensor. Actuat. Biol. Chem.*, Vol. 223, 45–51, 2016.
21. Shen, F., C. Wang, Z. Sun, K. Zhou, L. Zhang, and X. Shu, "Small-period long-period fiber grating with improved refractive index sensitivity and dual-parameter sensing ability," *Opt. Lett.*, Vol. 42, No. 2, 199–202, 2017.
22. Lu, H., S. Dai, Z. Yue, Y. Fan, H. Cheng, J. Di, D. Mao, E. Li, T. Mei, and J. Zhao, "Sb_2 Te_3 topological insulator: Surface plasmon resonance and application in refractive index monitoring," *Nanoscale*, Vol. 11, No. 11, 4759–4766, 2019.
23. Lu, J., D. Spasic, F. Delport, T. van Stappen, I. Detrez, D. Daems, S. Vermeire, A. Gils, and J. Lammertyn, "Immunoassay for detection of infliximab in whole blood using a fiber-optic surface plasmon resonance biosensor," *Anal. Chem.*, Vol. 89, No. 6, 3664–3671, 2017.
24. Lang, C., Y. Liu, K. Cao, and S. Qu, "Temperature-insensitive optical fiber strain sensor with ultra-low detection limit based oncapillary-taper temperature compensation structure," *Opt. Express*, Vol. 26, No. 1, 477, 2018.
25. Wang, Q., G. Farrell, and W. Yan, "Investigation on single-mode-multimode single-mode fiber structure," *J. Lightwave Technol.*, Vol. 26, No. 5, 512–519, 2008.
26. Geng, Y., X. Li, X. Tan, Y. Deng, and Y. Yu, "High-sensitivity Mach-Zehnder interferometric temperature fiber sensor based on a waist-enlarged fusion bitaper," *IEEE Sens. J.*, Vol. 11, No. 11, 2891–2894, 2011.
27. Yan, W., Q. Han, Y. Chen, H. Song, X. Tang, and T. Liu, "Fiber-loop ring-down interrogated refractive index sensor based on an SNS fiber structure," *Sensor. Actuat. Biol. Chem.*, Vol. 255, 2018–2022, 2018.
28. Wu, Q., Y. Semenova, P. Wang, and G. Farrell, "High sensitivity SMS fiber structure based refractometer — Analysis and experiment," *Opt. Express*, Vol. 19, No. 9, 7937–7944, 2011.